Journal of Physics D: Applied Physics

PAPER • OPEN ACCESS

Size and density control of skyrmions with picometer CoFeB thickness variations—observation of zero-field skyrmions and skyrmion merging

To cite this article: Christian Denker *et al* 2023 *J. Phys. D: Appl. Phys.* **56** 495302

OPEN ACCESS
IOP Publishing
Journal of Physics D: Applied Physics
J. Phys. D: Appl. Phys. **56** (2023) 495302 (11pp)
https://doi.org/10.1088/1361-6463/acf6cd

Size and density control of skyrmions with picometer CoFeB thickness variations—observation of zero-field skyrmions and skyrmion merging

Christian Denker[1], Sören Nielsen[2], Enno Lage[2], Malte Römer-Stumm[2], Hauke Heyen[1], Yannik Junk[1], Jakob Walowski[1], Konrad Waldorf[3], Markus Münzenberg[1,*] and Jeffrey McCord[2,4]

[1] Institut für Physik, Universität Greifswald, Felix-Hausdorff-Straße 6, 17489 Greifswald, Germany
[2] Department of Material Science, Nanoscale Magnetic Materials and Magnetic Domains, Kiel University, Kaiserstraße 2, 24143 Kiel, Germany
[3] Institut für Mathematik und Informatik, Universität Greifswald, Walther-Rathenau-Str. 47, 17487 Greifswald, Germany
[4] Kiel Nano, Surface and Interface Science (KiNSIS), Kiel University, Christian-Albrechts-Platz 4, 24118 Kiel, Germany

E-mail: markus.muenzenberg@uni-greifswald.de

Received 5 May 2023, revised 9 August 2023
Accepted for publication 5 September 2023
Published 15 September 2023

Abstract

The controlled formation and adjustment of size and density of magnetic skyrmions in Ta/CoFeB/MgO trilayers with low Dzyaloshinskii–Moriya interaction is demonstrated. Close to the out-of-plane to in-plane magnetic spin reorientation transition, we find that small energy contributions enable skyrmion formation in a narrow window of 20 pm in CoFeB thickness. Zero-field stable skyrmions are established with proper magnetic field initialization within a 10 pm CoFeB thickness range. Using magneto-optical imaging with quantitative image processing, variations in skyrmion distribution and diameter are analyzed quantitatively, the latter for sizes well below the optical resolution limit. We demonstrate the controlled merging of individual skyrmions. The overall demonstrated degree of comprehension of skyrmion control aids to the development of envisioned skyrmion based magnetic memory devices.

Supplementary material for this article is available online

Keywords: skyrmions, CoFeB, Kerr microscopy

(Some figures may appear in colour only in the online journal)

* Author to whom any correspondence should be addressed.

1. Introduction

Skyrme [1] predicted topologically stabilized wave objects to model nucleons in particle physics. They were termed skyrmions and exist in different media, including magnetic materials [2, 3]. Magnetic skyrmions were first observed by neutron diffraction in MnSi bulk material at cryostatic temperatures [4]. For magnetic thin films symmetry breaking by heavy metal/ferromagnetic (HM/FM) interfaces in conjunction with an additional oxidic or metallic layer [5] is used to introduce interfacial Dzyaloshinski–Moriya interaction (DMI), by which the formation of magnetic skyrmions is enabled in film systems with perpendicular magnetic anisotropy (PMA) [6]. In such thin film systems, skyrmions or skyrmion bubbles exist as circular magnetic structures with the central magnetization pointing opposite to its carrying magnetic matrix with a special domain wall configuration leading to a non-vanishing winding number. By this the skyrmions possess a topological charge [7]. Zero-field skyrmions were first detected in Fe/Ir thin films by spin-polarized scanning tunneling microscopy [8]. In addition, they provided the first evidence for the deterministic creation of individual skyrmions [9].

Magnetic films with PMA also form dipolar stabilized labyrinth or maze domains, but exhibit skyrmion bubbles in combination with out-of-plane (OOP) magnetic bias field application. Large skyrmions of several micrometers in diameter were generated at room temperature by the application of electrical currents in patterned HM/FM/oxide (HM/FM/Ox) trilayers [10] under the application of OOP magnetic bias fields. Inspired by this breakthrough, skyrmion bubbles at room temperature and their generation have been investigated for various magnetic thin film systems. Skyrmions could be established in single FM layer films based on HM/FM/Ox [10–15] and multilayers based on $(HM/FM)_n$ [16–20]. So far, zero-field skyrmions were generated only for multilayer structures [21, 22]. Yet, in a single FM layer external magnetic OOP bias fields are essential for the skyrmion stabilization [23]. Exceptions from this are limited to small patterned structures with an additional stabilization with the assistance of geometrical confinement in patterned nanostructures [12] due to magnetostatic interactions. Exchange biased systems provide a similar mechanism of stabilization [24].

The dependence of the skyrmion diameter with magnetic layer thickness and magnetic field relies on the subtle interplay of various energy contributions [25]. Close to the PMA to the in-plane magnetic anisotropy (IMA) spin reorientation transition, where the effective PMA approaches zero, the effect of DMI is dominating the magnetic texture and skyrmions develop. Their size decreases while advancing to the magnetic transition. Furthermore, modeling suggests that with increasing magnetic OOP field application the skyrmion size decreases until skyrmion annihilation at saturation (SAT). Thereby, the overall thickness range for the existence of skyrmions is very narrow with a high sensitivity of skyrmion properties to the FM film thickness. Yet, it is not clear how to nucleate skyrmions and how the transformation in skyrmion size takes place. The controlled nucleation of skyrmions is particularly of interest in conjunction with the alternatively and more regularly exhibited labyrinth domain state.

The intensive research activities on skyrmions are motivated by the quest for novel magnetic data storage solutions, with some resembling of historic magnetic bubble technology [26, 27]. First approaches were based on the shifting of magnetic domain walls by electrical currents in a resting host medium [28]. This idea was extended to the concept of a skyrmion racetrack memory [29] as the critical current densities for the movement of skyrmions are expected to be several orders smaller as compared to domain wall racetrack memories [30]. Alternative concepts for the application of skyrmions for stochastic computing schemes rely on the irreversible character of nucleation, movement, and annihilation of skyrmions by electrical means [23]. It has been shown that skyrmions can be created by electrical current pulses [10, 14, 17]. Especially, the topological properties of skyrmions enable a variable toolbox for the detection, creation, and annihilation of skyrmions [30–32]. Further, for the envisioned applications, an electrical write- and read-out scheme is necessary.

The most common skyrmion detection scheme is based on the topological Hall effect [33]. Alternatively, spin Hall magnetoresistance [34] or FM resonance measurements were applied for skyrmion detection [35]. Imaging techniques like spin polarized scanning tunneling microscopy at a low temperature around 4 K [9], electron microscopy (Lorentz transmission electron microscopy or scanning electron microscopy), synchrotron-based techniques using magnetic dichroism in the x-ray range, and magneto-optical Kerr effect (MOKE) imaging give direct access for the detection and investigation of skyrmion and skyrmion motion in various material systems (see, e.g. [3]). For envisioned practical applications spin transfer torque switching by magnetic tunnel junctions (MTJs) offers an efficient way for skyrmion creation and annihilation. In addition, MTJs provide a fast, scalable, and highly efficient option for skyrmion detection with excellent signal to noise ratio. MTJs for reading and writing of skyrmions have been proposed [36] and also realized experimentally [37]. For MTJs Ta/CoFeB/MgO/CoFeB is a suitable material system with a large tunnel magnetoresistance (TMR) ratio [38, 39].

Here, we investigate the possibilities of skyrmion stabilization by magnetic field in Ta/CoFeB/MgO, including the generation of zero-field skyrmions. The investigations are an important step for the implementation of skyrmion carrying layers in MTJs. A special focus is on the FM thickness range close to the spin reorientation transition with low effective PMA, where even small DMI dominates. We show that slightest variations in FM layer thickness have a drastic influence on the exhibited magnetic texture characteristics. Varying the average FM thickness by only a few picometers, strongly alters skyrmion properties in a systematic way. FM film thickness control on the picometer thickness level is essential for reliable magnetic field induced and zero-field stable skyrmion generation. Exact thickness selection allows an unprecedented degree of control over skyrmion characteristics. The presented study lays the foundation for skyrmion manipulation in spintronic devices.

2. Methods

In the following we demonstrate various ways of controlled skyrmion generation in the Ta/CoFeB/MgO material system. For that purpose, we investigated the parameter space for skyrmion generation close to the OOP (PMA) to IMA transition. This is the region of low PMA, where a general magnetic domain refinement occurs, and DMI effects become more prominent. An analysis of the influence of DMI to OOP anisotropy on the stability of skyrmions is found in [40]. A similar transition, but from (super)paramagnetic to PMA, is found for a lower FM thickness, where the formation of movable skyrmions due to paramagnetic instabilities is reported [41]. In that regime, also a reduced Curie temperature is exhibited. The chosen thicker FM-layer regime has the critical advantage that the thermal stability of skyrmions at room temperature for device applications is significantly increased.

To generate and investigate skyrmion behavior, we perform our experiments in CoFeB layers with a linear FM thickness gradient, resulting in a corresponding effective PMA gradient. This allows to study effects arising in a small average FM thickness window, corresponding to some picometers in CoFeB thickness variation. This enables us to study systematic variations of skyrmion properties without possibly occurring parameter variations due to small sample-to-sample variations.

Samples with a variation of CoFeB thickness (t_{CoFeB}) were grown on thermally oxidized Si(100) substrates in a ultrahigh vacuum (UHV) cluster system under the same optimized conditions as for the fabrication of Ta/CoFeB/MgO MTJs [42]. The CoFeB layers are prepared by magnetron sputtering deposition using growth rates of 0.045 nm s^{-1}, in Ar atmosphere at a pressure of 5×10^{-3} mbar and a base pressure around 5×10^{-10} mbar. The film thickness is monitored during deposition by a standard film thickness monitor using water cooled quartz crystals. High resolution transmission microscopy (HRTEM) measurements on similar structures showed a well-defined interface between the layers with some residual roughness [42]. To obtain a gradual thickness variation, the samples are mounted under an angle of 50° with respect to the sputter source normal. This geometric factor is resulting in a 20% linear increase of the CoFeB layer thickness along the substrate. The sputter target arrangement consequently results in an opposite wedged Ta layer growth (0.0078 nm s^{-1}) with the same thickness ratio along the wedge. A sample of Si(100)/500 nm SiO_2/5–3.7 nm (wedge) Ta/1.20–1.56 nm (wedge) $Co_{40}Fe_{40}B_{20}$/3.2 nm MgO/3 nm Ru was selected for the presented study. The schematics of the layer stack are shown in figure 1(a). The thickness gradient for a CoFeB film with an edge thickness of 1.2 nm is 0.028 nm mm^{-1}. For the Ta film with an edge thickness of 5 nm, the arrangement results in an opposite thickness gradient of -0.116 nm mm^{-1}. The MgO and Ru layers are deposited *in-situ* by e-beam evaporation in the UHV cluster with a base pressure in the range of 10^{-9} mbar and a deposition rate of 0.02 nm s^{-1}. The Ru layer prevents degradation of MgO at ambient atmosphere. *Ex-situ* annealing is performed in vacuum with a base pressure below 10^{-7} mbar for 1 h at final temperature. During the process of sample optimization, we tested several variations in the sample preparation and post-annealing. The sample to be investigated was annealed for 1 h at 60 °C to initialize the solid-state-epitaxy process at the MgO/CoFeB interface as for MTJs.

MOKE based magnetometry was used to extract local OOP magnetization loops. Complete sample MOKE imaging [43] was performed by a large-view MOKE microscope with Scheimpflug optics for further pre-characterization of the magnetic properties and for identifying the position of the PMA to IMA transition on the wedged layer samples. High-resolution MOKE microscopy [43] with variable and combined in-plane (IP) and OOP magnetic field application is used for the imaging of the skyrmion characteristics.

3. Results

3.1. Skyrmion generation and zero-field stable skyrmions

Figure 1(b) shows a large field-of-view MOKE microscopy image of the sample in the demagnetized state for a film thickness range increasing from $t_{\mathrm{CoFeB}} = 1.20$ nm to 1.44 nm. The linear FM thickness change over $\Delta t_{\mathrm{CoFeB}} = 0.24$ nm manifests itself in a gradual change in the magnetic domain size. With increasing FM thickness in the PMA region, the magnetic domain size shrinks, starting with some hundreds μm in size, down to below to the spatial resolution limit of the large-view MOKE microscope setup of about 10 μm. From the MOKE analysis the PMA to IMA transition is found to occur at $t_{\mathrm{CoFeB}} = 1.384$ (23) nm. Above this critical thickness only IP magnetic domain contrast and no OOP MOKE contrast is visible, while a strong OOP contrast and no IP contrast is observed below the CoFeB thickness of the PMA to IMA transition. The remanence magnetization M_r/M_s and coercive field H_c are nearly constant with $M_r/M_s = 1$ with $\mu_0 H_c \approx 0.6$–0.7 mT for a CoFeB thickness up to $t_{\mathrm{CoFeB}} = 1.35$ nm. The magnetic remanence decreases approaching the PMA to IMA transition (supplementary materials, figure S1). This is consistent with the formation of magnetic domains at zero field, which become favorable with decreasing effective PMA, approaching the IMA region. A corresponding linear MOKE signal amplitude change in the PMA regime is in accordance with a linear thickness variation FM wedge structure (supplementary materials, figure S1).

Example occurring magnetic domain structures are displayed in figures 1(c)–(f). Typical labyrinth (LP) domains occur at zero magnetic fields (figure 1(c)). An analysis of the labyrinth domain width in this CoFeB film thickness range shows clearly the expected strong decrease in domain width (supplementary materials, figure S2) [44, 45], due to the reduced effective PMA anisotropy strength and corresponding reduction of domain wall energy, also in combination with an existing DMI. A DMI value of $D = 0.11$ (0.01) mJ m^{-2} is determined from Brillouin light scattering (BLS) measurements around $t_{\mathrm{CoFeB}} \approx 1.3$ nm. With the application of OOP magnetic fields, the labyrinth domain phase transforms into a mixed (MP) labyrinth domain and skyrmion phase (SP) (figure 1(d)). With further increasing OOP magnetic

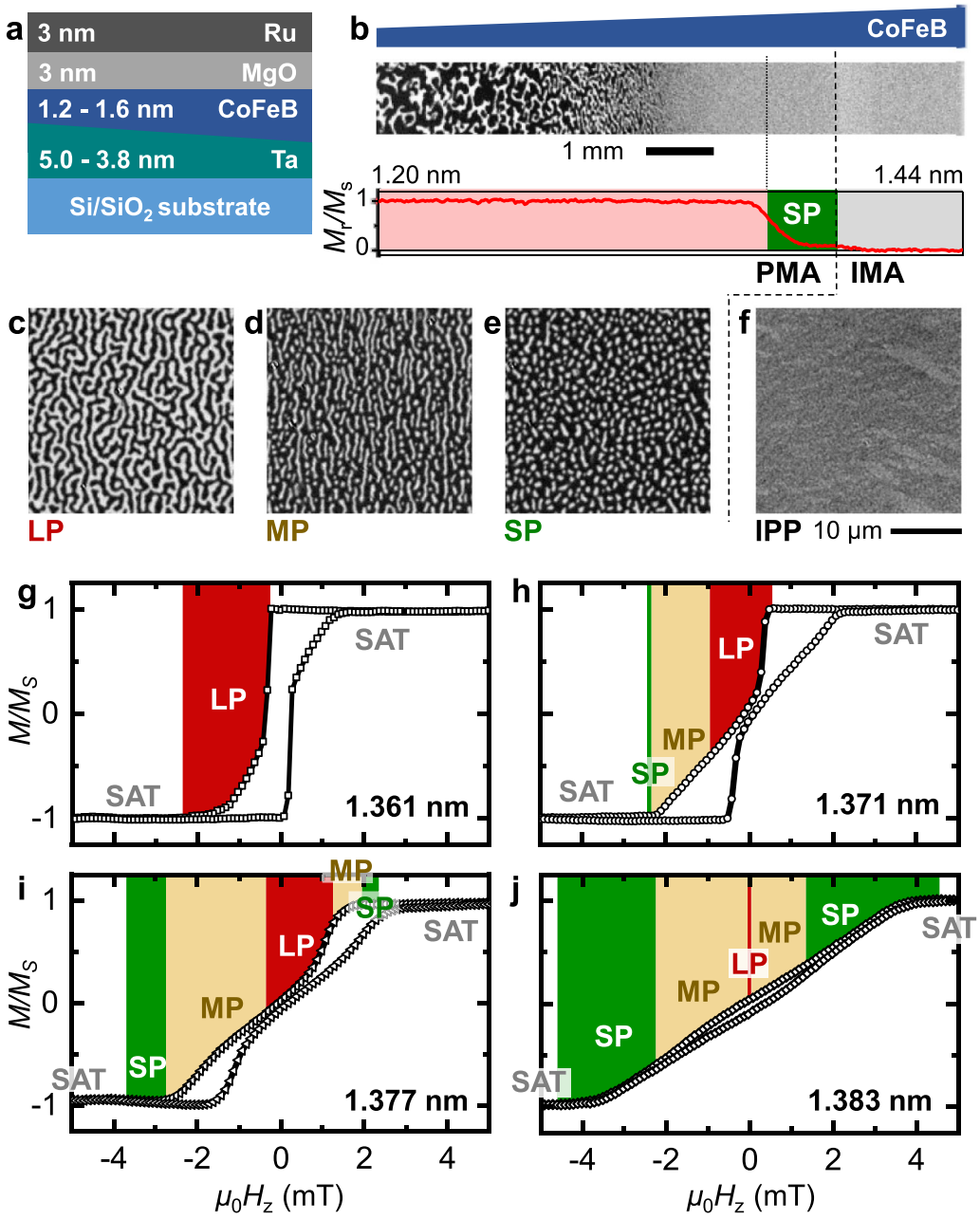

Figure 1. Magnetic domain evolution across the perpendicular magnetic anisotropy (PMA) to the in plane magnetic anisotropy (IMA) transition. (a) Sketch of the Si(100)/500 nm SiO_2/5–3.7 nm (wedge) Ta/1.20–1.56 nm (wedge) $Co_{40}Fe_{40}B_{20}$/3.2 nm MgO/3 nm Ru layer stack. (b) Overview MOKE microscopy image of the demagnetized state across the CoFeB wedge. The CoFeB thickness regime with PMA and IMA, as well as the thickness regime with skyrmions (SP) are indicated. (c)–(f) Exhibited magnetic domain states showing labyrinth domains (LP), mixed (MP) skyrmions and labyrinth, and pure skyrmion phases (SPs) (as indicated). (g)–(j) OOP magnetization loops at selected CoFeB thicknesses. The corresponding positions along the CoFeB wedge are indicated in (b). The regions of the observed domain phases during magnetization reversal are marked.

biasing fields a pure SP develops (figure 1(e)). The skyrmion nature of the developing magnetic texture is confirmed by its electrical current induced directional motion, showing a skyrmion Hall angle of close to 45° (supplementary materials, figure S3). This indicates a non-vanishing winding number of the skyrmion bubbles [46]. For higher CoFeB layer thickness IP magnetic domains with also weaker MOKE contrast (figure 1(f)), confirming the predominant IMA for higher CoFeB layer thicknesses.

In the PMA regime, the characteristics of the OOP magnetization curves display signatures of domain nucleation and annihilation. Example magnetization loops are displayed in figures 1(h)–(j). With increasing CoFeB thickness we find an increase in loop shearing and a corresponding decrease in hysteresis. The characteristic low PMA region in the narrow FM thickness range of $t_{CoFeB} = 1.361$ nm to 1.383 nm (over a nominal thickness variation of $\Delta t_{CoFeB} = 22$ pm) displays the nucleation and existence of narrow magnetic labyrinth

domains, as well as skyrmions during the magnetization reversal. The existence of different magnetic domain phases during magnetization reversal is indicated in the corresponding magnetization loops for the decreasing loop branch. Only labyrinth domains form for the lower thicknesses (figure 1(g), $t_{\mathrm{CoFeB}} = 1.361$ nm) during magnetization. With increasing CoFeB thickness (figure 1(h), $t_{\mathrm{CoFeB}} = 1.371$ nm), again labyrinth domains nucleate from magnetic SAT. Yet, further reversing the magnetic field, additional skyrmions start to nucleate. For the shown example labyrinth and skyrmion domains coexist for applied field amplitudes above $\mu_0 H_z \approx -1.0$ mT. Close to SAT ($\mu_0 H_z \approx -2.2$ mT), a pure skyrmion domain phase appears. With a further increase in the magnetic layer thickness by nominally $\Delta t_{\mathrm{CoFeB}} = 6$ pm the general magnetization loop characteristics remain (figure 1(i), $t_{\mathrm{CoFeB}} = 1.377$ nm). Yet, noteworthy alterations in the resulting domain pattern characteristics are observed. Pronounced regions with labyrinth, coexisting labyrinth and skyrmion phases, as well as with a pure SP, appear. Skyrmions start to appear for higher magnetic bias fields also before remanence. A further increase in t_{CoFeB} by just another $\Delta t_{\mathrm{CoFeB}} = 6$ pm increases the magnetic field range of an SP existence significantly (figure 1(j), $t_{\mathrm{CoFeB}} = 1.383$ nm). Concurrently, the magnetic field range for the appearance of the labyrinth domain phase is reduced to a very narrow field regime around $\mu_0 H_z \approx 0$ mT. The manifestation of the mixed magnetic texture and the pure SP is highly reproducible. Further increasing the CoFeB thickness results in an IP magnetic domain alignment due to an effective IMA (see also figure 1(c-4)).

An overview of the manifestations of labyrinth and especially the SPs with CoFeB thickness during magnetization reversal is summarized in the experimental phase diagram shown in figure 2(a), where the different regimes of magnetic texture existence are indicated. Only the variation with decreasing field from positive SAT is shown. Starting from negative SAT the phase diagram is inverted in terms of the magnetic field values. For OOP magnetic field applications three distinct regions are identified. Region LP represents the labyrinth phase and appears with small magnetic fields for all the considered film thicknesses. This region overlaps with region mixed phase (MP), showing the coexistence of labyrinth and skyrmions for a film thickness exceeding $t_{\mathrm{CoFeB}} \approx 1.370$ nm and magnetic fields below $\mu_0 H_z \approx 1$ mT. This region partly overlaps with SP, which marks the parameter space for exclusive skyrmion formation, starting at film thicknesses above $t_{\mathrm{CoFeB}} = 1.375$ nm and magnetic fields exceeding about $\mu_0 H_z \approx 1.5$ mT in amplitude. At this thickness skyrmions exist around and below SAT field, but no zero field skyrmions occur.

The skyrmion formation can be further initiated by changes in magnetic history also in other ways. By combining OOP magnetic fields with IP magnetic field pulse application additional and different regions of skyrmion stability are obtained. An overview is given in figure 2(b). Combining IP magnetic field application with small OOP magnetic fields results in a mixture of labyrinth domain and skyrmion phases ($\mathrm{MP_p}$). Pure SPs are obtained with higher additional OOP magnetic field application ($\mathrm{SP_p}$). The range of OOP magnetic field amplitude H_z for the different regimes is indicated. Skyrmions are generated for lower CoFeB thicknesses as compared to magnetic reversal. Yet, the range of magnetic bias field of around $\mu_0 H_z \approx 1.25$ mT for pure skyrmion occurrence is very narrow for $1.360\ \mathrm{nm} \leqslant t_{\mathrm{CoFeB}} \leqslant 1.375\ \mathrm{nm}$ ($\Delta t_{\mathrm{CoFeB}} = 5$ pm). With increasing t_{CoFeB}, this is also reflected in an increase in the magnetic SAT field (see also figures 1(g)–(j)), the narrow band of occurrence widens up significantly toward magnetic fields ranging $1.5\ \mathrm{mT} < \mu_0 H_z < 5$ mT. This regime is still similar to the reversal behavior. None of the field applications lead to an entirely zero-field SP.

Yet, by applying slightly off-axis IP magnetic saturation fields and reducing the magnetic field, the nucleation and stabilization of a pure zero-field SP ($\mathrm{SP_0}$) in a narrow thickness range above and below $t_{\mathrm{CoFeB}} = 1.375$ nm is attained as indicated in figure 2(c). The existence of pure zero-field skyrmions in our single FM film structures is limited to a narrow CoFeB thickness window of about $\Delta t_{\mathrm{CoFeB}} \approx 10$ pm. Similar magnetic history schemes for the prevention of the energetically slightly preferred labyrinth domain nucleation using IP magnetic field applications are known from PMA ferrite films [47]. For larger thicknesses still in the PMA regime and by demagnetizing the sample with an OOP magnetic field application, we obtain a zero-field mixed skyrmion and labyrinth phase ($\mathrm{MP_0}$) only in a narrow CoFeB thickness regime. No pure zero-field SP is obtained in this thickness regime.

3.2. Skyrmion size and density control

In addition to the existence of skyrmions, the skyrmion properties are also altered dependent on the magnetic field conditions. In the following, we discuss the dependence of skyrmion size and density as a function of t_{CoFeB} and OOP magnetic field application. For that, we use MOKE intensity evaluation to determine the skyrmion diameter d_{sky} of multiple skyrmions from the MOKE micrographs, allowing for a statistically relevant study of skyrmion behavior for large skyrmion populations.

From the MOKE micrographs, the magnetic texture image analysis is performed using ImageJ 1.51g, including the Fiji image processing packages [48]. A standard segmentation algorithm with an intensity threshold to separate the individual domains and distinguish between the MOKE image regions, belonging to a skyrmion, and the surrounding magnetic matrix is used for automated skyrmion density and size analysis. For the quantitative analysis the micrographs are evaluated using the standard Fiji function for particle analysis [48]. The obtained MOKE contrast is related to the magnetization $m = M/M_s$, which is obtained by normalizing to the maximum MOKE contrast derived from the local MOKE intensity difference $MO_{\pm}$ between up and down magnetized magnetic domains, corresponding to the magnetization amplitude $\pm M_s$. The integral MO skyrmion intensity I is then equal to

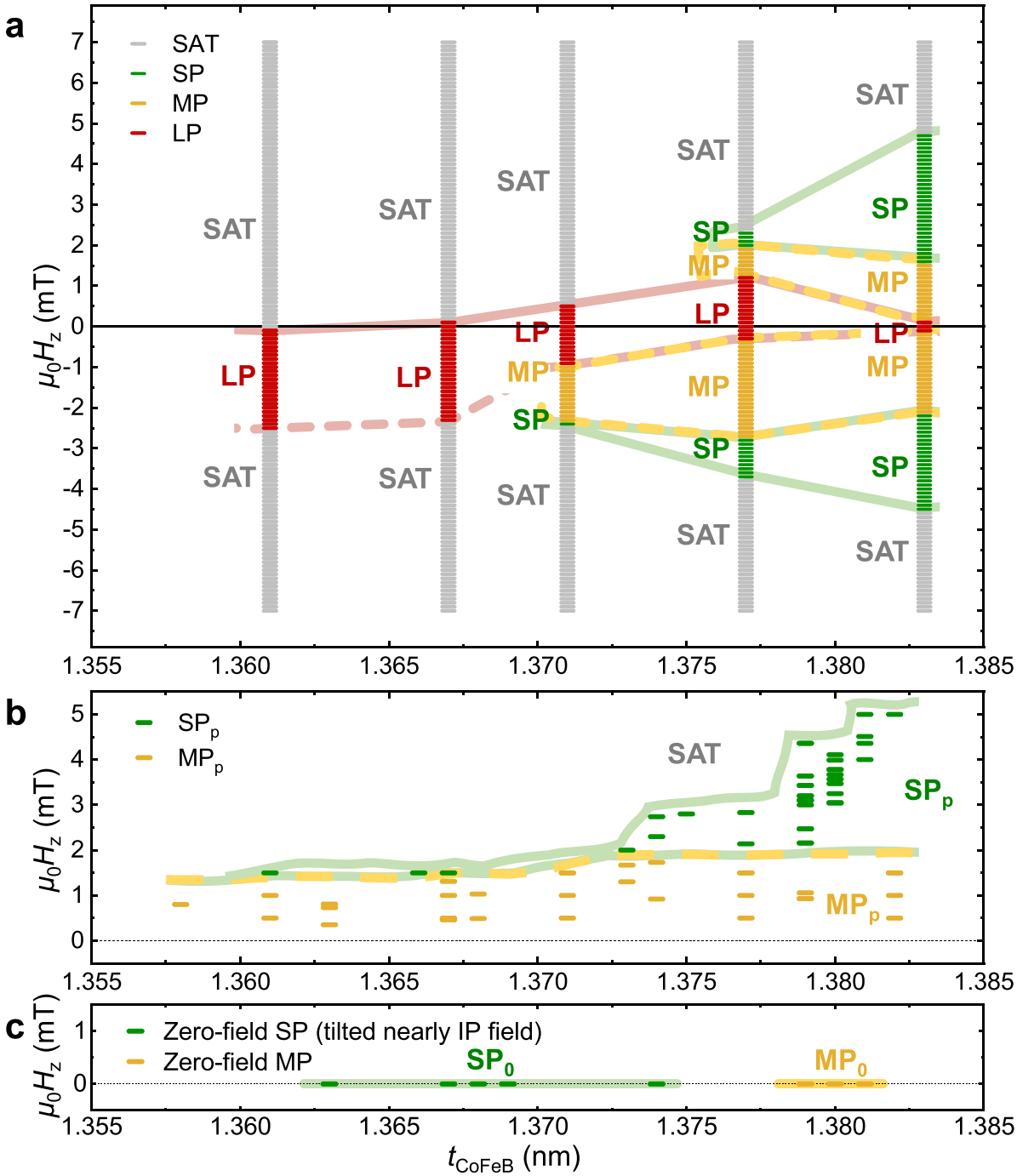

Figure 2. Phase diagrams of magnetic textures at the perpendicular magnetic anisotropy region (PMA) to the in plane magnetic anisotropy region (IMA). (a) Phase diagram during magnetization reversal with OOP magnetic field variation. **SP**: skyrmions appearing directly by OOP field variation, **MP**: labyrinth domains and skyrmions forming directly by OOP field variation, **LP**: labyrinth domains from OOP field variation. **SAT** corresponds to a saturated magnetic state. (b) Phase diagram for skyrmions generated by IP magnetic pulses with a concurrent OOP bias field: $\mathbf{MP_p}$: labyrinth domains and skyrmions, $\mathbf{SP_p}$: pure skyrmion phase. (c) Zero-field skyrmion stabilization. $\mathbf{MP_0}$: mixed labyrinth domains and skyrmions at zero magnetic field, $\mathbf{SP_0}$: stable pure skyrmion domain states at zero field. Pure zero-field skyrmion states are induced by decreasing a slightly tilted nearly IP magnetic field to zero.

$I = A\,MO_{\pm}$, with $MO_{\pm}$ being the MOKE intensity difference between up and down magnetization normalized to its area A. For a skyrmion we assume $A = 1/4\ \pi\ d_{sky}$, from which we derive the skyrmion diameter d_{sky}. The integral MO intensity is independent of the domain wall width, any blur by imaging optics or applied digital Gaussian noise filters, because the equi-magnetization line of 50% defines the skyrmion diameter d_{sky} under the assumption of symmetric domain walls. Taking the normalization into account, the intensity threshold that corresponds to the magnetic skyrmion matrix is adjusted manually. The applied method is similar to the technique used for the determination of integral domain wall widths in soft

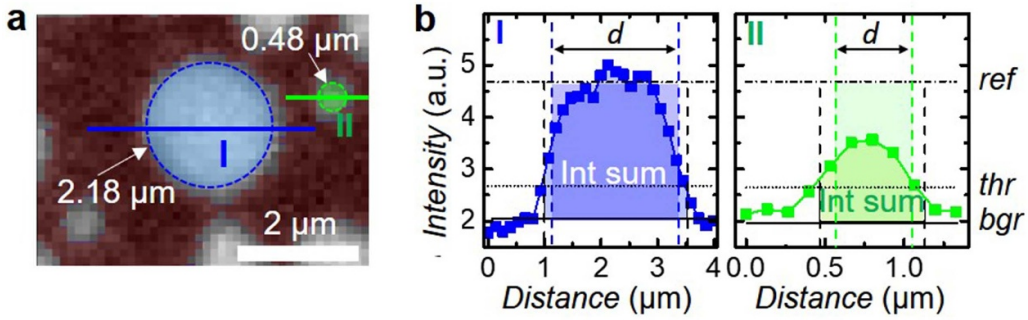

Figure 3. Image analysis by threshold segmentation and size determination by integrated MO intensity beyond the Abbe limit. (a) MOKE image with pixels below the threshold shaded dark reddish. The determined diameters for two exemplary skyrmions are indicated by shaded circles with dashed outlines in blue ($d_{sky} = 2.18$ μm) and green ($d_{sky} = 0.48$ μm). (b) Corresponding line intensity plots as indicated in (a). The background intensity (*bgr*), corresponding to the magnetic matrix MO intensity, and the threshold intensity (*thr*) applied for the automated analysis are indicated. The average maximum intensity for a fully opposite magnetization to the matrix is shown as the shaded area below the curves to visualize the integrated intensity. The shaded rectangles display the determined skyrmion diameter, taking the difference from the measured intensity maximum to the maximum (*ref*) signal into account.

magnetic samples [49] and skyrmion diameters in HM/FM multilayers [50]. The method enables the comprehensive evaluation of the variation of skyrmion diameters, density, and distribution of large skyrmion ensembles.

An exemplary size analysis of two skyrmions of different diameters is sketched in figure 3. The threshold (*thr*) is chosen as close as possible to the average magnetic matrix MOKE intensity to include the maximum of image pixels for the intensity sum for the derivation of skyrmion size, but high enough to allow for reliable separation of the magnetic matrix background (*bgr*) from the image noise. The threshold of detection is kept at a minimal level to minimize the error of the diameter determination from noise in the (in this case) low MOKE intensity values. By this scheme, additional noise contributions increase the variation of the border of the detected skyrmion diameter, but generally retain the average diameter. Accordingly, the noise level of the imaging system and the distance between the skyrmions define the minimum detectable diameter of skyrmions. In our experiments the reliable automated skyrmion diameter detection limit is around $d_{sky} \approx 100$ nm. This is well below the spatial resolution of the MOKE microscopy images of approx. 300 nm for the numerical aperture (NA = 0.9) of the used objective lens. The automatic image evaluation allows analysis of multiple skyrmions from a single magnetic domain image. In our case, up to hundreds of skyrmions per MOKE image could be analyzed and the corresponding skyrmion densities and sizes were extracted.

Results of the analysis of the OOP magnetic field behavior are summarized for a fixed CoFeB film thickness of $t_{CoFeB} = 1.379$ nm in figures 4(a)–(d). Starting from a zero-field labyrinth domain structure, a mixture of labyrinth domains and skyrmions appear at an OOP field of about $\mu_0 H_z = 1$ mT (figure 4(a-1)). With further increasing the magnetic field, the density of labyrinth domains reduces with a consequential increase in the skyrmion density to a maximum density of about $\rho_{sky} \approx 1$ μm^{-2} at $\mu_0 H_z = 2$ mT (figure 4(b)). This first initial behavior is due to the replacement of the labyrinth by the skyrmion bubble phase [16, 27]. A stable pure SP forms for larger fields (figures 4(a-2) and (a-3)) and remains until magnetic saturation. Within that regime, increasing the OOP field results in a reduction of the skyrmion density ($\rho_{sky} = 0.06$ μm^{-2} at $\mu_0 H_z = 3.7$ mT). Concurrently, the average skyrmion diameter decreases continuously from $d_{sky} \approx 400$ nm at $\mu_0 H_z = 1$ mT to $d_{sky} \approx 160$ nm (figure 4(c)). Yet, the skyrmion diameters are not constant but distributed (figure 4(d)) with a standard deviation from $d_{\sigma-sky} = 100$ nm down to $d_{\sigma-sky} = 50$ nm. Coinciding with the reduction in average skyrmion size, the degree of the skyrmion size distribution is decreasing.

The minimum attainable skyrmion size approaching the PMA to IMA transition in the CoFeB film thickness range from $t_{CoFeB} \approx 1.361$–1.382 nm is investigated next. The skyrmions were initialized by an IP field pulse application under an OOP magnetic bias field. We show in figures 4(e)–(h) the size and density dependence as a function of CoFeB thickness along the boundary between skyrmion and saturated magnetization state in the phase diagram (see figure 2(b)). Accordingly, the OOP magnetic field is increased to the maximum for each position with the ability to observe skyrmions along this stability line. Exemplary MOKE images showing isolated skyrmions are displayed in figure 4(e). The variance in the skyrmion density shown in figure 4(f) is strongly dependent on how close the OOP magnetic field is relative to the critical field for skyrmion annihilation. With the fast decreasing PMA, the average skyrmion diameter d_{sky}, shown in figure 4(g), decreases with increasing t_{CoFeB} from $d_{sky} = 750$ nm at $t_{CoFeB} = 1.361$ nm and $\mu_0 H_z = 0.8$ mT to $d_{sky} = 135$ nm at $t_{CoFeB} = 1.382$ nm and $\mu_0 H_z = 5$ mT. This is accompanied by a decrease in the skyrmion diameter variation from about $d_{\sigma-sky} = 210$ nm down to $d_{\sigma-sky} = 40$ nm. The extracted size distribution shows a clear cut-off at the resolution limit of the automated skyrmion identification algorithm at $d_{sky} = 85$ nm for the highest CoFeB thickness and accordingly the smallest skyrmion diameter. Yet, the derived size distribution (figure 4(h)) indicates the existence of even smaller skyrmions, the diameter value of which is not accessible by our systematic analysis procedure.

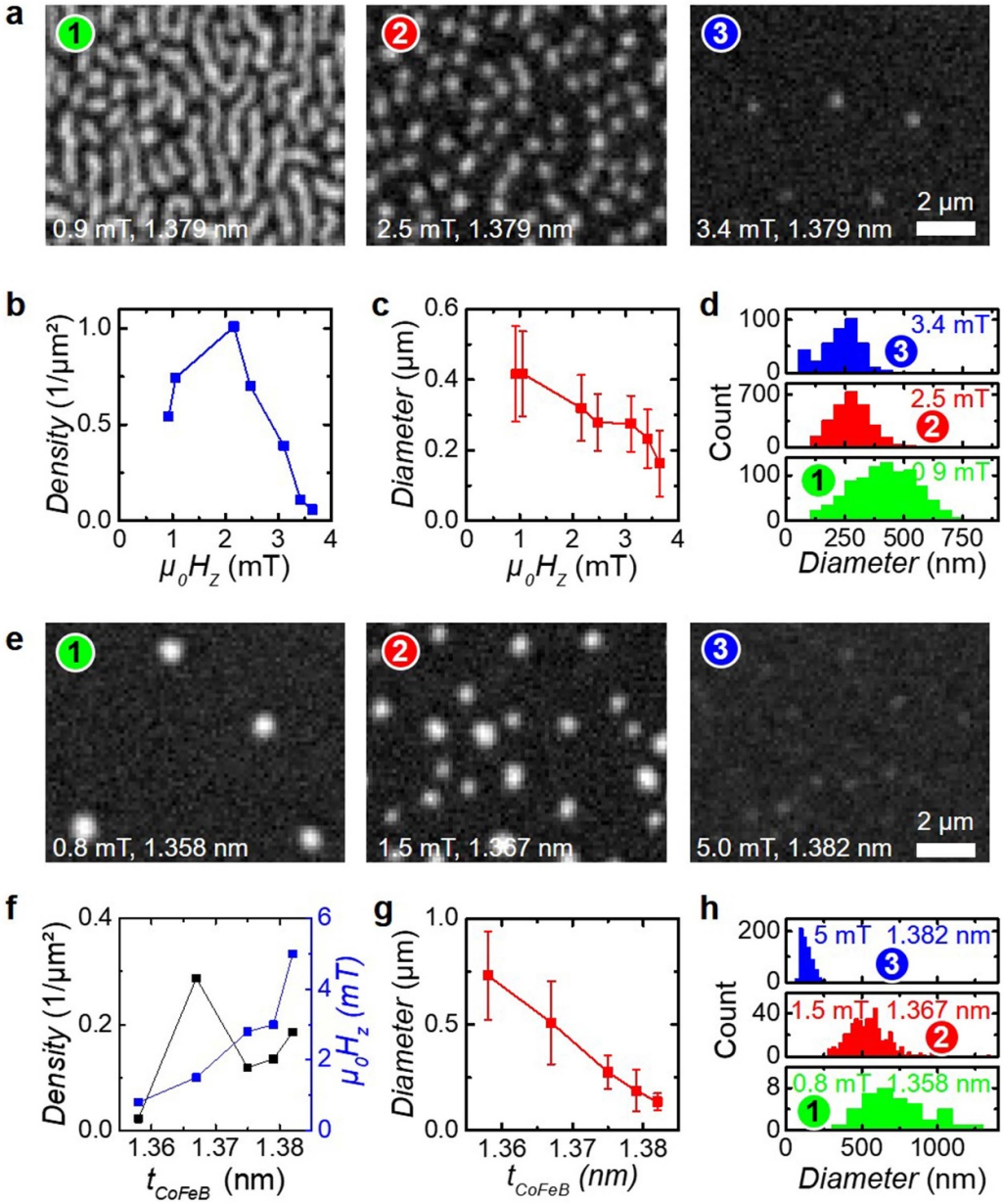

Figure 4. Large skyrmions ensemble analysis: magnetic field and thickness. Magnetic domains induced by the application of IP magnetic field pulses as function of the OOP bias field at a CoFeB thickness of 1.379 nm: (a) MOKE microscopy images for an OOP magnetic bias field of $\mu_0 H_z = 0.9$ mT, 2.5 mT, and 3.4 mT as indicated. The brightness and contrast were adjusted to cover the range from the minimum background intensity to the maximum bright intensity. (b) Skyrmion density and (c) diameter as a function of the applied OOP magnetic bias field. The error bars show the standard deviation of the obtained skyrmion diameter distribution. (d) Corresponding histograms of the skyrmion diameter distributions. Magnetic domains induced by application of IP magnetic field pulses as function of the CoFeB thickness with the OOP magnetic field close to instability: (e) MOKE microscopy images at a CoFeB thickness of 1.379 nm for OOP bias field of $\mu_0 H_z = 0.8$ mT, 1.5 mT, and 5.0 mT. (f) Skyrmion density and corresponding OOP magnetic field amplitude as a function of CoFeB thickness. (g) Skyrmion diameter changes with CoFeB thickness. The error bars show the standard deviation of the skyrmion diameter distribution. (h) Corresponding histograms of the skyrmion diameter distributions.

3.3. Skyrmion state transformations

In general, a multi-skyrmion state should be controllably formed by starting from skyrmions and merging them by interaction to multi-skyrmion solitons. Assuming topological protection, the total topological charge of the merged topological soliton is expected to be the sum of the individual topological charges. This is backed up by a mathematical analysis of the spherical topology [51] in a so-called baby-Skyrme model (for a numerical example for five solitons, each of charge $n = 1$, relaxing to multi-skyrmions with higher charges see supplementary materials, figure S4).

The high degree of control of skyrmion size and density in the wedged sample system by selecting the skyrmion state with picometer CoFeB thickness resolution, allows us to use it to form a multi-skyrmion state and to study their interaction.

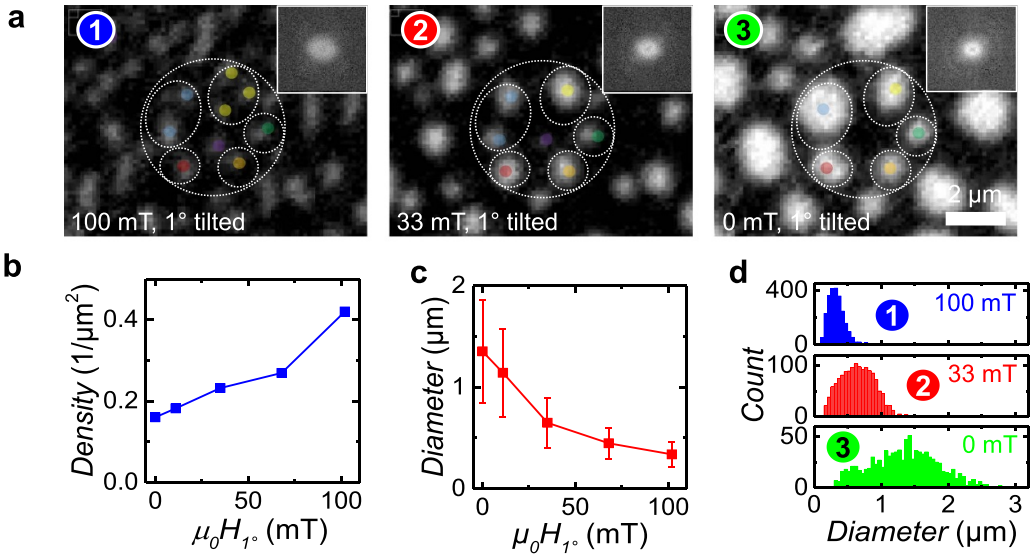

Figure 5. (a) Process of skyrmion merging at a CoFeB thickness of 1.363 nm during decreasing a 1° tilted nearly IP magnetic field down to zero field. Magnetic field values are indicated. The MOKE images' brightness and contrast are adjusted for better skyrmion visibility. The colored spots and dashed circles mark groups of skyrmions, which coalesce during the procedure. (b) Skyrmion density and (c) skyrmion diameter as a function of applied magnetic field. (d) Skyrmion diameter distributions for the three bias field values of (a). The error bars in (c) correspond to the standard deviation of the diameter distributions (see also (d)).

To realize a similar state to the described multi-skyrmion model in a real-world sample, we have chosen a CoFeB thickness regime, where the generation of zero-field skyrmions is achieved. The application of a $\mu_0 H_1{}^\circ \approx 100$ mT nearly IP magnetic field (tilted OOP by 1°) results in skyrmions for t_{CoFeB} ranging from 1.363 nm to 1.374 nm. This corresponds the SP_0 phase shown in figure 2(c). With the close to IP applied field the nucleation of skyrmions with high density is dominated by magnetization rotation and especially a continuous skyrmion transformation down to zero field is exhibited. The corresponding development of skyrmions with reduction of a slightly tilted IP magnetic field to the remanent skyrmion state is shown in figure 5. The OOP field component below which skyrmions are observed is around $\mu_0 H_z = 2$ mT. This is within the range of skyrmion existence with pure OOP field application. However, reducing the applied field to zero preserves the initial SP (figures 5(a-1)–(a-3)). The decrease in the applied magnetic field is accompanied by an increase in skyrmion size together with a decrease in skyrmion density. While the skyrmion density decreases from $\rho_{\mathrm{sky}} \approx 0.40\ \mu\mathrm{m}^{-2}$ to $\rho_{\mathrm{sky}} \approx 0.16\ \mu\mathrm{m}^2$ (figure 5(b)), the average diameter increases from $d_{\mathrm{sky}} = 0.34\ \mu\mathrm{m}$ to $d_{\mathrm{sky}} = 1.35\ \mu\mathrm{m}$ (figure 5(c)). This forces the coalescence of skyrmions. For better illustration, traced skyrmions are color coded in figure 5(a). We assume the same starting charge for all skyrmions, since we know that all show the same direction of the skyrmion Hall angle close to 45° (supplementary materials, figure S4). The observed merging behavior resembles aspects of the numerical predictions. Our results clearly indicate homogenous growth as it is expected for random coalescence. Moreover, we find that the thermal diffusion is low and the lifetimes of the (metastable) skyrmions in the range of several hours to days.

4. Conclusion

The appearance of magnetic skyrmions with varying size and density is demonstrated in Ta/CoFeB/MgO trilayers. The system mimics the bottom electrode and tunnel barrier of an MTJ. Using a CoFeB thickness wedge structure enables precise and continuous magnetic anisotropy tuning. By this, we were able to stabilize skyrmions close to the PMA to IMA transition. Skyrmions appear as part of OOP magnetic field variation within a narrow CoFeB thickness window ($t_{\mathrm{CoFeB}} = 1.370$–$1.383$ nm) at zero magnetic field up to around OOP fields of $\mu_0 H_z \approx 4.5$ mT. Skyrmion generation by IP magnetic field pulses extends the parameter range for skyrmion existence in terms of thickness and magnetic field regime. For both approaches of skyrmion existence an experimental phase diagram is derived. The skyrmion diameter and density can be controlled by the effective anisotropy varying with CoFeB film thickness and the external magnetic bias field. The average diameter is adjustable from below 100 nm skyrmion diameter up to about 1.4 μm, while the density can be freely tuned from around 1 $\mu\mathrm{m}^{-2}$ to single skyrmion density. The merging of skyrmions with magnetic field application is observed, qualitatively resembling predictions of a baby-Skyrme model.

Zero-field stable skyrmions in single structures are stabilized by a setting routine comprising the application of nearly IP magnetic fields. The possibility of allowing for controllable adjustment of single domain and skyrmion states at zero fields together with the high stability of the states, the observed long skyrmion lifetimes, and appropriate pinning, demonstrates the general suitability of the material system and the tunability of skyrmion properties for magnetic memory applications.

Data availability statement

The data cannot be made publicly available upon publication because the cost of preparing, depositing and hosting the data would be prohibitive within the terms of this research project. The data that support the findings of this study are available upon reasonable request from the authors.

Acknowledgments

The project was initially financially supported by the 'Bund Norddeutscher Universitäten' and later funded by the German Research Foundation (DFG) through the Priority Program SPP 2137 Skyrmionics: 'Topological Spin Phenomena in Real-Space for Applications'. We thank P Mazalski, I Sveklo, and A Maziewski for determining the DMI value. J M and M M thank K Brandenburg for proof-reading of the manuscript.

ORCID iDs

Markus Münzenberg https://orcid.org/0000-0002-1332-5678
Jeffrey McCord https://orcid.org/0000-0003-0237-6450

References

[1] Skyrme T H R 1962 A unified field theory of mesons and baryons *Nucl. Phys.* **31** 556–69
[2] Jiang W, Chen G, Liu K, Zang J, te Velthuis S G E and Hoffmann A 2017 Skyrmions in magnetic multilayers *Phys. Rep.* **704** 1–49
[3] Fert A, Reyren N and Cros V 2017 Magnetic skyrmions: advances in physics and potential applications *Nat. Rev. Mater.* **2** 17031
[4] Mühlbauer S, Binz B, Jonietz F, Pfleiderer C, Rosch A, Neubauer A, Georgii R and Böni P 2009 Skyrmion lattice in a chiral magnet *Science* **323** 915–9
[5] Ajejas F, Sassi Y, Legrand W, Collin S, Thiaville A, Garcia J P, Pizzini S, Reyren N, Cros V and Fert A 2022 Interfacial potential gradient modulates Dzyaloshinskii-Moriya interaction in Pt/Co/metal multilayers *Phys. Rev. Mater.* **6** L071401
[6] Rössler U K, Bogdanov A N and Pfleiderer C 2006 Spontaneous skyrmion ground states in magnetic metals *Nature* **442** 797–801
[7] Bogdanov A N and Rössler U K 2001 Chiral symmetry breaking in magnetic thin films and multilayers *Phys. Rev. Lett.* **87** 37203
[8] Heinze S, von Bergmann K, Menzel M, Brede J, Kubetzka A, Wiesendanger R, Bihlmayer G and Blügel S 2011 Spontaneous atomic-scale magnetic skyrmion lattice in two dimensions *Nat. Phys.* **7** 713–8
[9] Romming N, Hanneken C, Menzel M, Bickel J E, Wolter B, von Bergmann K, Kubetzka A and Wiesendanger R 2013 Writing and deleting single magnetic skyrmions *Science* **341** 636–9
[10] Jiang W *et al* 2015 Blowing magnetic skyrmion bubbles *Science* **349** 283–6
[11] Litzius K *et al* 2017 Skyrmion Hall effect revealed by direct time-resolved x-ray microscopy *Nat. Phys.* **13** 170–5
[12] Boulle O *et al* 2016 Room-temperature chiral magnetic skyrmions in ultrathin magnetic nanostructures *Nat. Nanotechnol.* **11** 449–54
[13] Jaiswal S *et al* 2017 Investigation of the Dzyaloshinskii-Moriya interaction and room temperature skyrmions in W/CoFeB/MgO thin films and microwires *Appl. Phys. Lett.* **111** 22409
[14] Schott M, Bernand-Mantel A, Ranno L, Pizzini S, Vogel J, Béa H, Baraduc C, Auffret S, Gaudin G and Givord D 2017 The skyrmion switch: turning magnetic skyrmion bubbles on and off with an electric field *Nano Lett.* **17** 3006–12
[15] Duong N K, Raju M, Petrović A P, Tomasello R, Finocchio G and Panagopoulos C 2019 Stabilizing zero-field skyrmions in Ir/Fe/Co/Pt thin film multilayers by magnetic history control *Appl. Phys. Lett.* **114** 072401
[16] Yu G *et al* 2016 Room-temperature creation and spin-orbit torque manipulation of skyrmions in thin films with engineered asymmetry *Nano Lett.* **16** 1981–8
[17] Woo S *et al* 2016 Observation of room-temperature magnetic skyrmions and their current-driven dynamics in ultrathin metallic ferromagnets *Nat. Mater.* **15** 501
[18] Soumyanarayanan A *et al* 2017 Tunable room-temperature magnetic skyrmions in Ir/Fe/Co/Pt multilayers *Nat. Mater.* **16** 898–904
[19] Moreau-Luchaire C *et al* 2016 Additive interfacial chiral interaction in multilayers for stabilization of small individual skyrmions at room temperature *Nat. Nanotechnol.* **11** 444–8
[20] Hrabec A, Sampaio J, Belmeguenai M, Gross I, Weil R, Chérif S M, Stashkevich A, Jacques V, Thiaville A and Rohart S 2017 Current-induced skyrmion generation and dynamics in symmetric bilayers *Nat. Commun.* **8** 15765
[21] Brandão J, Dugato D A, Seeger R L, Denardin J C, Mori T J A and Cezar J C 2019 Observation of magnetic skyrmions in unpatterned symmetric multilayers at room temperature and zero magnetic field *Sci. Rep.* **9** 4144
[22] Li M, Rai A, Pokhrel A, Sapkota A, Mewes C, Mewes T, De Gra Ef M and Sokalski V 2020 Formation of zero-field skyrmion arrays in asymmetric superlattices *Appl. Phys. Lett.* **117** 112403
[23] Zázvorka J *et al* 2019 Thermal skyrmion diffusion used in a reshuffler device *Nat. Nanotechnol.* **14** 658–61
[24] Gaurav Rana K *et al* 2020 Room-temperature skyrmions at zero field in exchange-biased ultrathin films *Phys. Rev. Appl.* **13** 044079
[25] Bernand-Mantel A, Camosi L, Wartelle A, Rougemaille N, Darques M and Ranno L 2018 The skyrmion-bubble transition in a ferromagnetic thin film *SciPost Phys.* **4** 027
[26] Chikazumi S and Graham C D (ed) 2010 *Physics of Ferromagnetism* 2nd edn *repr. with corr* (*International Series of Monographs on Physics 94*) (Oxford University Press)
[27] Malozemoff A P, Slonczewski J C and Wolfe R 1979 *Magnetic Domain Walls in Bubble Materials: Advances in Materials and Device Research* (Elsevier)
[28] Parkin S S P, Hayashi M and Thomas L 2008 Magnetic domain-wall racetrack memory *Science* **320** 190–4
[29] Fert A, Cros V and Sampaio J 2013 Skyrmions on the track *Nat. Nanotechnol.* **8** 152–6
[30] Koshibae W, Kaneko Y, Iwasaki J, Kawasaki M, Tokura Y and Nagaosa N 2015 Memory functions of magnetic skyrmions *Jpn. J. Appl. Phys.* **54** 53001
[31] Kang W, Huang Y, Zheng C, Lv W, Lei N, Zhang Y, Zhang X, Zhou Y and Zhao W 2016 Voltage controlled magnetic skyrmion motion for racetrack memory *Sci. Rep.* **6** 23164
[32] Zhang X, Zhou Y, Ezawa M, Zhao G P and Zhao W 2015 Magnetic skyrmion transistor: skyrmion motion in a voltage-gated nanotrack *Sci. Rep.* **5** 11369
[33] Maccariello D, Legrand W, Reyren N, Garcia K, Bouzehouane K, Collin S, Cros V and Fert A 2018 Electrical detection of single magnetic skyrmions in

metallic multilayers at room temperature *Nat. Nanotechnol.* **13** 233–7
[34] Aqeel A, Azhar M, Vlietstra N, Pozzi A, Sahliger J, Huebl H, Palstra T M, Back C H and Mostovoy M 2021 All-electrical detection of skyrmion lattice state and chiral surface twists *Phys. Rev.* B **103** L100410
[35] Satywali B, Kravchuk V P, Pan L, Raju M, He S, Ma F, Petrović A P, Garst M and Panagopoulos C 2021 Microwave resonances of magnetic skyrmions in thin film multilayers *Nat. Commun.* **12** 1–8
[36] Bhattacharya D, Al-Rashid M M and Atulasimha J 2016 Voltage controlled core reversal of fixed magnetic skyrmions without a magnetic field *Sci. Rep.* **6** 31272
[37] Guang Y, Zhang L, Zhang J, Wang Y, Zhao Y and Tomasello R 2022 Electrical detection of magnetic skyrmions in a magnetic tunnel junction *Adv. Electron. Mater.* **9** 2200570
[38] Mathon J and Umerski A 2001 Theory of tunneling magnetoresistance of an epitaxial Fe/MgO/Fe(001) junction *Phys. Rev.* B **63** 220403(R)
[39] Ikeda S, Hayakawa J, Ashizawa Y, Lee Y M, Miura K, Hasegawa H, Tsunoda M, Matsukura F and Ohno H 2008 Tunnel magnetoresistance of 604% at 300K by suppression of Ta diffusion in CoFeB/MgO/CoFeB pseudo-spin-valves annealed at high temperature *Appl. Phys. Lett.* **93** 82508
[40] Aranda A R, Hierro-Rodriguez A, Kakazei G N, Chubykalo-Fesenko O and Guslienko K Y 2018 Magnetic skyrmion size and stability in ultrathin nanodots accounting Dzyaloshinskii-Moriya exchange interaction *J. Magn. Magn. Mater.* **465** 471–9
[41] Srivastava T, Lim W, Joumard I, Auffret S, Baraduc C and Béa H 2019 Mapping different skyrmion phases in double wedges of Ta/FeCoB/TaOx trilayers *Phys. Rev.* B **100** 220401(R)
[42] Leutenantsmeyer J C *et al* 2015 Spin-transfer torque switching at ultra low current densities *Mater. Trans.* **56** 1323–6
[43] McCord J 2015 Progress in magnetic domain observation by advanced magneto-optical microscopy *J. Phys. D: Appl. Phys.* **48** 333001
[44] Kooy C and Enz U 1960 Experimental and theoretical study of the domain configuration in thin layers of $BaFe_{12}O_{19}$ *Philips Res. Rep.* **15** 7–29
[45] Maziewski A, Zablotskii V and Kisielewski M 2002 Analysis of magnetic domain sizes in ultrathin ferromagnetic films *Phys. Status Solidi* a **189.3** 1001–5
[46] Nagaosa N and Tokura Y 2013 Topological properties and dynamics of magnetic skyrmions *Nat. Nanotechnol.* **8** 899–911
[47] Kojima H and Gotō K 1965 Remanent domain structures of $BaFe_{12}O_{19}$ *J. Appl. Phys.* **36** 538–43
[48] Schindelin J *et al* 2012 Fiji: an open-source platform for biological-image analysis *Nat. Methods* **9** 676–82
[49] Pfannenmüller J, Rave W and Hubert A 1988 Measuring the surface domain wall width by magnetooptic methods *12th Int. Coll. on Magnetic Films and Surfaces, Le Creusot* pp 156–7
[50] Soldatov I V, Jiang W, Te Velthuis S G E, Hoffmann A and Schäfer R 2018 Size analysis of sub-resolution objects by Kerr microscopy *Appl. Phys. Lett.* **112** 262404
[51] Weidig T 1999 The baby Skyrme models and their multi-skyrmions *Nonlinearity* **12** 1489